Slow-Sound-Based Delay-Line Acoustic Metamaterial

M. Malléjac,[1,*] P. Sheng,[2] V. Tournat,[1] V. Romero-García,[1] and J.-P. Groby[1]

[1] *Laboratoire d'Acoustique de l'Université du Mans (LAUM), UMR 6613, Institut d'Acoustique - Graduate School (IA-GS), CNRS, Le Mans Université, France*

[2] *Department of Physics, HKUST, Clear Water Bay, Kowloon, Hong Kong, China*

(Received 6 December 2021; revised 22 February 2022; accepted 25 March 2022; published 19 April 2022)

Periodic structures composed of quarter-wavelength or Helmholtz resonators have been widely used in the design of acoustic metamaterials. An interesting phenomenon achievable through hybridization in such structures is the slow sound, which results from the strong dispersion produced by the local resonances. It gives rise to many applications such as deep subwavelength sound absorbers or metadiffusers. All the applications proposed so far have been analyzed only in the frequency domain (steady state). In this work, we propose a passive treatment that can be used in room acoustics, which requires considering the time domain and all multiple reflections. We analytically design a delay line from a metasurface made of Helmholtz resonators, using slow-sound propagation. We prove numerically and experimentally that such structures can delay a pulse and thus reproduce the sound perception of a propagation over a given distance, larger than the actual size of the treatment. The limitations of real-time pulse propagation, dispersion, and losses on audio fidelity are discussed.

DOI: 10.1103/PhysRevApplied.17.044035

I. INTRODUCTION

The control of acoustic waves for room acoustics applications has been of constant interest for centuries, for two main purposes: to control diffusion and to enhance absorption. From the first Helmholtz resonators used in antique amphitheaters and Shroeder's diffusers principle [1], a long road has been traveled to more sophisticated systems such as active electroacoustic devices [2,3], virtual sources and immersive boundaries [4–7], optimized graded porous materials [8], or acoustic metasurfaces and metamaterials [9–14]. The great advantage of the latter is that they offer the possibility of tackling the device thickness-frequency paradigm. A thickness greater than the quarter of the acoustic wavelength is usually required to attain a good efficiency for both phenomena, absorption or diffusion. In particular, Yang *et al.* defined a causality-dictated inequality stating the optimal absorption spectrum as a function of sample thickness [15], which inevitably leads to a compromise between working frequency bandwidth and thickness. It is worth noting here, that Mak *et al.* proposed a design based on soft boundaries to go beyond this causal limit [16].

The search for deep subwavelength sound absorption has been one of the main avenues for the development of acoustic metamaterials and metasurfaces [10,17,18]. Several strategies have been employed to address this challenge, both in transmission [11,18–21] and reflection [22–24] problems: soft boundaries [16], decorated membrane panels [25–27], bubble metascreens [28,29], Helmholtz [19,22,26,30,31] and coiled-up [15,17,32–34] resonator arrangements, among others. Of particular interest is the phenomenon of slow sound [23,35,36], resulting from the strong dispersion around the resonances of the system. It allows both the sound speed and the inherent losses to be adjusted simply by changing the geometry and properties of the resonators.

Diffusion control using metasurfaces [37] has also attracted much interest and, in particular, Jimenez *et al.* have designed a metadiffuser based on Helmholtz resonators (HRs) capable of controlling the phase of the reflection coefficient of a surface and thus modifying the diffusion pattern [38]. An experimental proof of this design was performed by Ballestero *et al.* [12,39].

Despite all this research based on slow sound, realistic applications, especially in the time domain, have not been thoroughly studied.

In this work, we propose to study analytically and numerically, to design and fabricate, and then to experimentally validate a delay-line device allowing to time delay a pulse. We first outline the paradigm underlying this work and study the influence of the geometry on the effective and scattering properties of the system. We then discuss the challenge of temporal propagation in such metamaterials and explain the design strategy employed.

*matthieu.mallejac@univ-lemans.fr

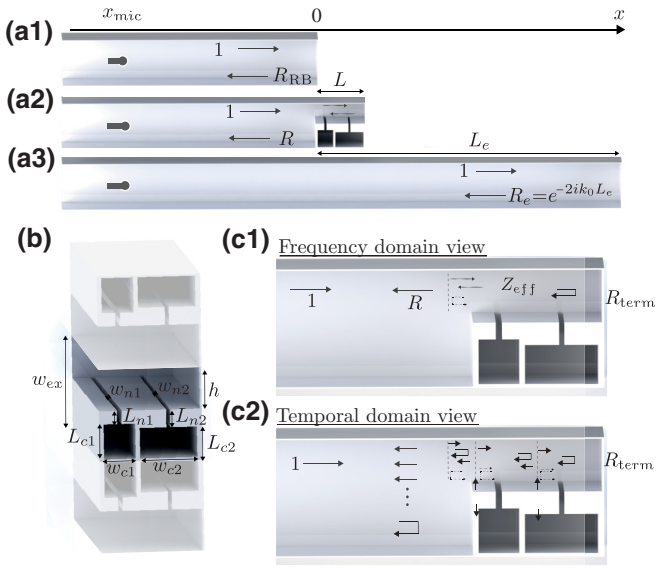

FIG. 1. (a) Schematics of the different configurations measured in a square cross-section impedance tube of width w_{ex}, in which a plane wave is impinging from the left and is reflected on a rigid wall: (a-1) configuration without the metadevice, i.e., empty tube, (a-2) configuration with the metamaterial of length L placed at the end of the rigidly backed tube, and (a-3) target configuration to be reproduced with the metamaterial. (b) Geometrical dimension of the Helmholtz resonators. (c) Differences between the permanent (frequency) regime view and the temporal propagation view.

Finally, we show numerical simulation and experimental results of our delay line for three different configurations.

II. CONCEPT AND SYSTEM: PERMANENT REGIME APPROACH

The idea behind this work is to propose a device to be placed on the walls of a room as sketched in Fig. 1, allowing to give a sound sensation of a room larger than it really is, which is also referred to as an acoustic mirage by Norris [40]. In other words, we seek to control the phase ϕ_R of the reflection coefficient R, and thus to be able to tune the apparent group delay τ_g

$$\tau_g(\omega) = -\frac{d}{d\omega}\phi_R(\omega), \tag{1}$$

with ω being the angular frequency.

Since a pulse is by definition finite in time, its frequency content spreads to some extent. Thus, in order for the metasurface to delay the pulse without distorting it significantly, it must have a near-constant group delay, i.e., a near-linear phase, over the bandwidth of the pulse.

For this purpose, we consider a metasurface composed of Helmholtz resonators mounted in parallel to a slit opened to the room and backed by a rigid wall. For sake of simplicity, we show here a one-dimensional (1D) situation consisting of two different HRs of dimensions given in Fig. 1(b) and Table I, placed in a square cross-section impedance tube of width $w_{ex} = 149$ mm. The walls of the impedance tube being rigid, i.e., Neumann condition applies, the considered configuration is equivalent to an infinite symmetric repetition of the unit cell as depicted in Fig. 1(b).

The strong dispersion generated in the slit above the resonators allows careful monitoring of the real and imaginary parts of the wave number $k(\omega)$, and thus of the group velocity $c_g = d\omega/d\mathrm{Re}\{k(\omega)\}$ and dissipation [$\propto \mathrm{Im}\{k(\omega)\}$].

The dispersion by a one HR unit cell is calculated in steady state by the transfer-matrix method (TMM) (see Appendix C) and depicted in Figs. 2(a) and 2(b) by the dotted lines. This dispersion relation does not account for the finite size of the system under study since it is derived directly from the transfer-matrix elements of a single unit cell. The finite size effects of the system can be seen by additionally calculating the reflection and transmission coefficient of the entire device and then deriving the effective properties (see Appendix C for more details). The effective wave number and group velocity derived from the scattering parameters are thus shown in Figs. 2(a)–2(c). It is worth noting here, that the rigid backing, i.e., $\partial p/\partial x = 0$, imposes a mirror symmetry. The effective medium corresponding to a rigidly backed system of N resonators is equivalent to an effective medium of $2N$ resonators in transmission.

The slow-sound phenomenon, which is driven by the resonator geometry, is clearly visible in Fig. 2(c), with a subsonic group velocity in the static limit ($\omega \to 0$) and decreasing until the stop band above the HR resonance (colored in gray). In parallel, the dissipation increases near the stop band of the system, as shown by the large imaginary part of the wave number in Fig. 2(b). For a given geometry, i.e., resonance frequency, we are therefore able to work with a given group velocity and amount of loss, just by selecting the frequency.

The phase of the metasurface reflection coefficient is plotted with the group delay in Figs. 2(d) and 2(e) for $N = 1$ or 2 identical resonators (dashed and dotted-dashed black lines). Each resonator gives rise to a -2π phase jump and a group delay peak at frequencies corresponding to the Fabry-Perot resonances of the finite-depth structure. The case of two detuned resonators is also represented by the red solid lines. Although the periodicity is broken, we still have the same behavior with two group delay peaks at frequencies related to the resonance frequency of each resonator. The choice of different resonators thus facilitates the design of a metasurface with a quasiflat group delay. The two group delay maxima are located in the vicinity of the open stop bands above the resonance frequency of each different HR. Note here that the sharp peaks in Fig. 2

TABLE I. Dimensions of the metasurface for the different configurations considered.

Configurations	w_{ex}	h	w_{c1}	L_{c1}	w_{n1}	L_{n1}	a_1	w_{c2}	L_{c2}	w_{n2}	L_{n2}	a_2
HRs, dispersion relation	149 mm	68.8 mm	21.4 mm	29.1 mm	13.1 mm	45.2 mm	25.5 mm	46.7 mm	11.9 mm	2.5 mm	61.2 mm	60.7 mm
Config. 1—L_e = 1 m	149 mm	65.8 mm	51.3 mm	56.7 mm	7.8 mm	57 mm	92.7 mm	49.5 mm	28.7 mm	6.6 mm	28.7 mm	102.9 mm
Config. 2—L_e = 0.75 m	149 mm	65.8 mm	31.3 mm	56.7 mm	7.8 mm	37 mm	56.6 mm	49.5 mm	28.7 mm	6.6 mm	28.7 mm	66.8 mm
Config. 3—L_e = 0.6 m	149 mm	65.8 mm	21.6 mm	56.7 mm	7.8 mm	27.3 mm	38.9 mm	49.5 mm	28.7 mm	6.6 mm	28.7 mm	49.1 mm

(c) result from the inverse of the partial derivative of the nonzero flat wave number ($c_g = d\omega/d\mathrm{Re}\{k\}$), due to the folding of the dispersion relation, in the frequency ranges between the stop bands. These regions are therefore also highly dissipative [see Fig. 2(b)]. A compromise must be found to reproduce both the right amount of loss and the time delay of a propagation over the target length.

III. TIME DOMAIN OPTIMIZATION

Although effective properties and total reflectance are a good way to model and design structures in the steady state (as generally done for metamaterials and metasurfaces), they are not suitable for the time domain, as they do not account for the first reflection interferences of the transient regime required to reach the steady state. Under the steady-state condition (frequency-domain view), the design strategy would consist of imposing both an impedance matching condition and a target group delay over a given frequency range by controlling the effective impedance and total reflection. Impedance matching ensures that all of the incident wave will be transmitted into the slit, propagate with a low group velocity, be reflected back by the rigid wall, and propagate back. The wave is therefore efficiently time delayed due to the slow sound, as illustrated in Fig. 1(c-1). In contrast, treating the time domain requires considering the reflection at each interface that are hidden in frequency calculations since only the total reflection is considered. In particular, the mere presence of a cross-section change at $x = 0$ generates a

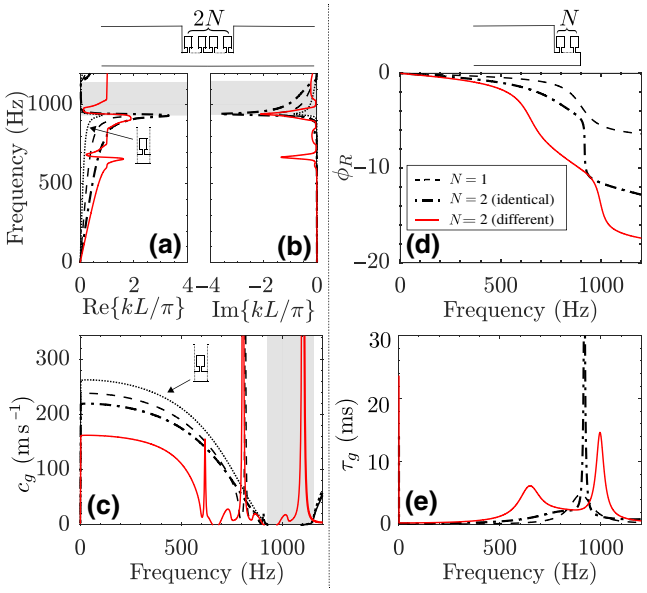

FIG. 2. Analytically calculated effective properties of the metasurface. (a) Real and (b) imaginary parts of the normalized dispersion relation, and (c) effective group velocity. The dotted lines represent the one unit-cell effective parameters (infinite device) while the dashed, dotted-dashed, and red solid curves represent the effective parameters accounting for the finite size of the device, respectively, for $N = 1$, $N = 2$ with two identical unit cells, and $N = 2$ with two different HRs. (d) Phase of the reflection coefficient and (e) group delay in the rigidly backed configuration.

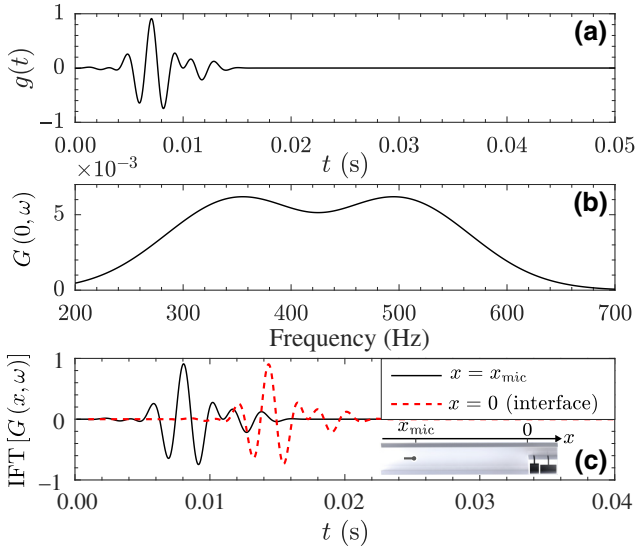

FIG. 3. Pulse under consideration: (a) temporal signal of the pulse, (b) spectral content, and (c) propagated pulse at $x = x_{\mathrm{mic}} = -2.6$ m, black solid line, and at the interface $x = 0$, red dashed line.

first direct reflection, which cannot be delayed in time, as the reflected energy does not enter the metasurface.

Therefore, the design strategy adopted here is to optimize the geometry directly in the time domain for a given time propagating pulse and to use destructive interferences to minimize unwanted reflections (direct reflection at $x = 0$ and coda) and to maximize desired reflections in order to preserve the shape of the delayed pulse.

The considered pulse, see Fig. 3(a), consists of a combination of two cosine-modulated Gaussian pulses with carrier frequencies 350 and 500 Hz. The metasurface must therefore be efficient on the challenging low-frequency range shown in Fig. 3(b). We can then calculate the propagated pulse via an inverse Fourier transform (IFT) of the initial pulse multiplied by the total reflection coefficient sought R. As an example, we show on Fig. 3(c) the pulse at the microphone position (black line) and at the interface ($x = 0$) after a propagation on a length of $x_{\text{mic}} = 2.6$ m (red dotted line).

To mimic the propagation of the $g(t)$ pulse over a length L_e with our device, we optimize the geometry of its resonators by minimizing the difference between the target delayed pulse IFT $\left[G(\omega)\, e^{-2ik_0 L_e}\right]$ and the propagated pulse in the metasurface, modeled by its total reflection coefficient calculated by TMM, i.e., IFT $[G(\omega)\, R_{\text{TMM}}]$, where $G(\omega) = \text{FT}[g(t)]$.

IV. RESULTS

Figure 4 illustrates the steady-state scattering properties of the optimized metasurface reproducing a

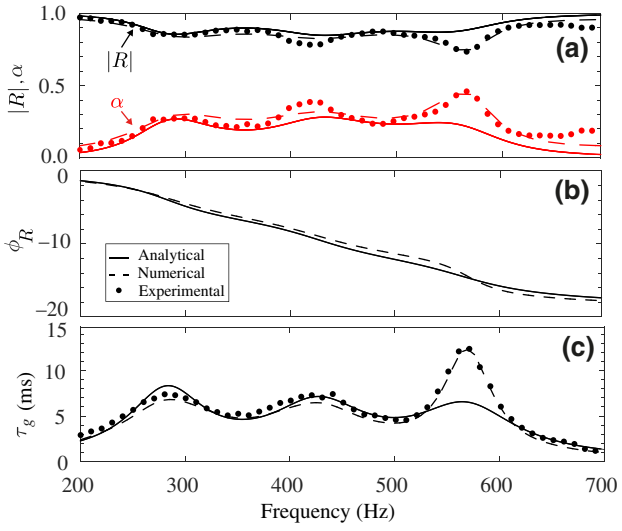

FIG. 4. Steady-state scattering properties of the metasurface optimized to reproduce a $L_e = 1$ m. (a) Reflection magnitude (black) and absorption coefficient (red), (b) phase of the reflection coefficient, and (c) apparent group delay. Solid lines represent the analytical results (TMM), dashed lines the numerical results, and dots the experimental results.

distance of 1 m and the corresponding group delay. The dimensions of the 16-cm-thick metasurface of the optimized geometry are given in Table I. A twofold procedure is used to validate the TMM modeling. On the one hand, we numerically model the metasurface with a three-dimensional (3D) finite-element model using the viscothermal module of COMSOL Multiphysics software. A fine mesh is required for the boundary layers of all the rigid walls (cavity, neck, slit) to account for the viscothermal losses in the device with good accuracy. On the other hand, an experimental validation is performed. The metasurface is machined with 3-mm-thick aluminum plates and is placed in a $w_{\text{ex}} = 149$ mm square impedance tube with a rigid backing. The scattering properties are recovered from the measurement of the microphone-to-speaker frequency responses at four-microphone positions. The agreement between the analytical (solid), numerical (dashed line), and experimental (dots) results is very good, thus validating our analytical modeling used for the optimization process. The slight discrepancies visible around 580 Hz can be attributed to the length correction modeling for the Helmholtz resonators (see Appendix A).

Figure 5(a-3) shows the numerically simulated and experimentally measured outgoing temporal wave from the device. As expected and predicted by the analytical results given in Fig. 5(a-2), the pulse is effectively delayed by 5.8 ms. This delay, highlighted by the gray horizontal arrow, corresponds to the time difference between the pulse after propagation in the metasurface and after reflection at the interface (metasurface replaced by a rigid backing at $x = 0$) shown, respectively, in Figs. 5(a-3,4). Slight discrepancies are visible at the starting and end of the pulse (both in the experiments and in the simulations) and are due to several unavoidable limitations. First, although the optimization is performed over a frequency region where the dispersion is small, the Helmholtz resonator metasurfaces remain dispersive, as shown by the nonperfectly constant group delay in Fig. 5(a-1). Second, destructive interference with early and late reflections cannot perfectly result in total wave cancellation. In addition, due to the viscothermal losses inherent to Helmholtz resonators, the amplitude of the pulse is slightly reduced. Finally, the second pulse visible in Fig. 5(a-4) is due to the reflection on the rigid wall around the loudspeaker. Nevertheless, most of the energy remains concentrated on the targeted pulse and therefore has the potential to give the overall good feeling of a delayed pulse.

From the optimized geometry mimicking the 1-m-long configuration, we then optimize the geometry to reproduce two other propagation distances $L_e = 0.75$ m and $L_e = 0.6$ m, by changing only the cavity widths w_c by a factor 0.611 and 0.42, respectively. The device thicknesses for these two configurations are therefore $L = 9.8$ cm and $L = 6.6$ cm, respectively. The dimensions of the three configurations are given in Table I and the results are given

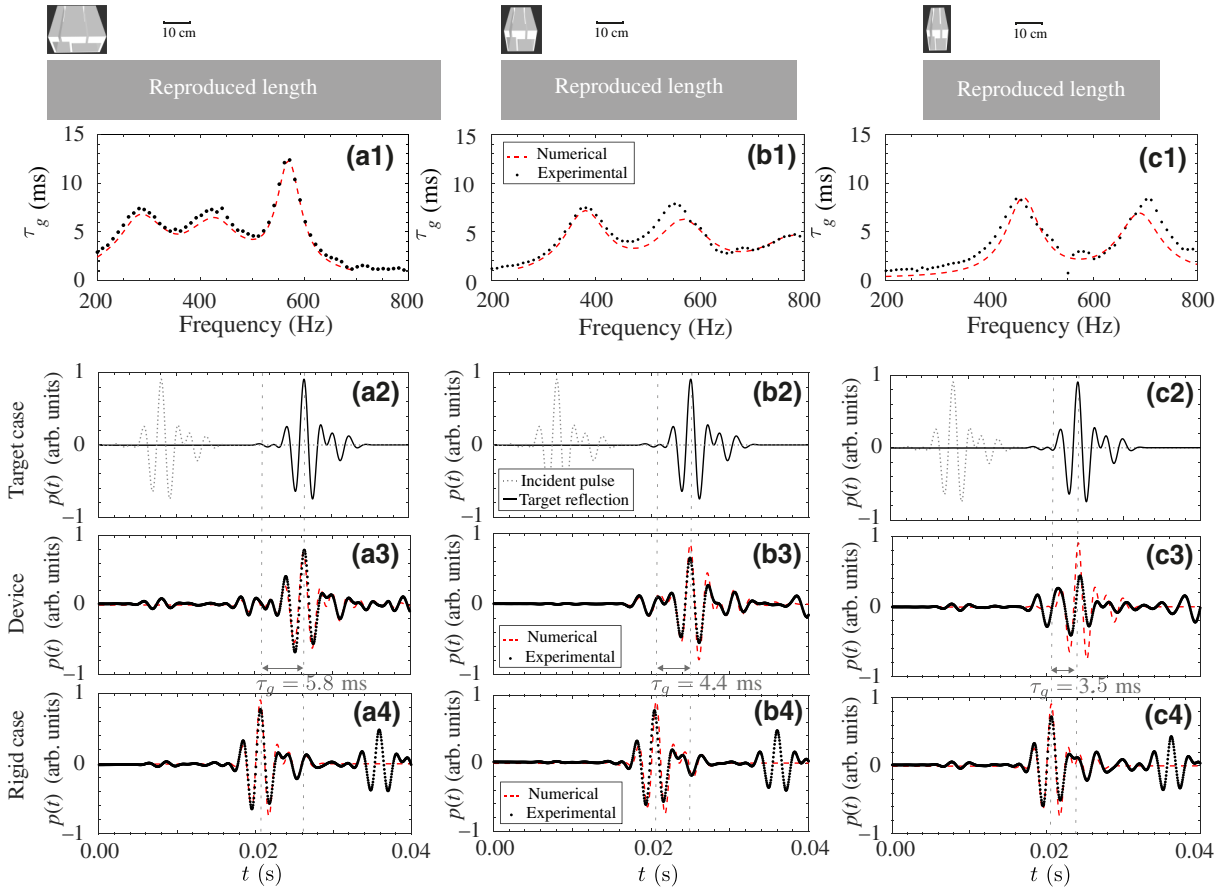

FIG. 5. Metasurface delayed pulse for the three configurations considered: $L_e = 1$ m (a), 0.75 m (b), and 0.6 m (c). (-1) steady-state group delay, (-2) incident and target pulse (analytical), (-3) measured and simulated pulse delayed by the metasurface, and (-4) measured and simulated pulse reflected off a rigid wall (without metasurface). The red dashed lines and black dots represent the full-wave simulation and experimental results, respectively. The solid black lines represent the analytical target, and the thin black dotted lines the incident pulse.

in Figs. 5(b) and 5(c). In each case, the optimal geometry delays the pulse by the correct time delay, $\tau_g = 4.4$ ms and 3.5 ms, respectively. We can see that the steady-state group delay of the optimized geometry corresponds to these values at frequencies 350 and 500 Hz, i.e., the two carrier frequencies of the pulse. Although the pulse is distorted more significantly when we linearly reduce the geometry from the first configuration, the shape and location of the pulse matches the target values. Note again here that the second pulse visible in the last row of subplots is solely due to the experimental setup. The left side of the impedance tube, on which the source is mounted, is not anechoic, which leads to a back reflection of the reflected pulse.

V. CONCLUSION

In conclusion, we analytically design in this work a metasurface capable of temporally delaying a pulse. This subwavelength device is able to mimic a propagation over a distance much larger than its thickness L, i.e., $L_e \approx 6.25L$ for the first configuration, $L_e \approx 7.8L$ for the second, and $L_e \approx 9L$ for the third configuration and could be reconfigurable, since a linear modification of an initial geometry can reproduce several distances. As room acoustics application requires to account for the multiple reflections at each interface, the geometry optimization is performed by minimizing in the time domain the difference between the targeted pulse (propagation over a distance L_e) and the pulse after propagation in the metasurface of reflection coefficient R, determined from the TMM. We validate our analytical predictions both numerically and experimentally. We find that all three configurations reproduce well the correct group delay at the two carrier frequencies of the considered pulse and thus that the center of the pulse corresponds well to that of the target. Small discrepancies at the beginning and end of the delayed pulses, due to unavoidable dispersion and unwanted reflection, are found. However, since most of the energy of the pulse is concentrated in its center, which matches well with that

of the target, the device could provide the sound feeling of the delayed pulse. This work focuses only on the 1D delay-line case. It is worth noting that in room acoustics sound is expected to be incident from a range of arbitrary angles of incidence, i.e., the problem is then at least two dimensional (2D). Going to 2D raises a number of questions and constraints related to the local impedance strategy employed in our design, as well as the conditions that must be satisfied for all angles, namely impedance matching, the Snell-Descartes law, and identical travel times. A workaround to this problem is to design anisotropic effective properties as proposed in Ref. [40], which constitutes possible perspectives for this work. In terms of additional prospects, a reconfigurable accordion device could be fabricated and the bandwidth of the working frequency could be extended, for example, by adding multiple slits in parallel.

ACKNOWLEDGMENTS

This work is funded by the Metaroom Project No. ANR-18-CE08-0021 and co-funded by ANR and RCG.

APPENDIX A: ANALYTICAL MODELING

The metasurface is analytically modeled using the transfer matrix $\mathbf{T}$, which relates the state vectors $\mathbf{W} = (p, vS)^T$ on each side of the medium

$$\mathbf{W}(0) = \mathbf{T}\mathbf{W}(d) = \begin{bmatrix} t_{11} & t_{12} \\ t_{21} & t_{22} \end{bmatrix} \mathbf{W}(d), \tag{A1}$$

with p the acoustic pressure, v the particle velocity, and S the section of the waveguide.

The transfer matrix

$$\mathbf{T} = \mathbf{T}_{\Delta_{\text{slit}}} \left[\mathbf{T}_{a_1} \mathbf{T}_{\text{HR}_1} \mathbf{T}_{a_1} \mathbf{T}_{a_2} \mathbf{T}_{\text{HR}_2} \mathbf{T}_{a_2} \right], \tag{A2}$$

is built from the multiplication of elementary matrices representing the propagation over a distance $a_{1,2}/2$ (subscripts $_{\cdot 1,2}$ are not written in the following for readability)

$$\mathbf{T}_{\mathbf{a_{1,2}}} = \begin{bmatrix} \cos\left(\frac{k_s a}{2}\right) & iZ_s \sin\left(\frac{k_s a}{2}\right) \\ iZ_s^{-1} \sin\left(\frac{k_s a}{2}\right) & \cos\left(\frac{k_s a}{2}\right) \end{bmatrix}, \tag{A3}$$

and of the transfer matrix of the Helmholtz resonator, in parallel to the duct, and assumed to be pointlike

$$\mathbf{T}_{\mathbf{HR_{1,2}}} = \begin{bmatrix} 1 & 0 \\ 1/Z_{\text{HR}} & 1 \end{bmatrix}. \tag{A4}$$

Z_{HR} is the acoustic impedance of a Helmholtz resonator of length and width of neck and cavity L_n, w_n, L_c, and w_c, respectively, and reads as follows [41]:

$$Z_{\text{HR}} = -i \frac{\cos(k_n L_n)\cos(k_c L_c) - Z_n k_n \Delta l \cos(k_n L_n)\sin(k_c L_c)/Z_c - Z_n \sin(k_n L_n)\sin(k_c L_c)/Z_c}{\sin(k_n L_n)\cos(k_c L_c)/Z_n - k_n \Delta l \sin(k_n L_n)\sin(k_c L_c)/Z_c + \cos(k_n L_n)\sin(k_c L_c)/Z_c}. \tag{A5}$$

k_n, k_c and Z_n, Z_c are, respectively, the characteristic wave numbers and impedances of the neck and cavity of the resonators. A correction length $\Delta l = \Delta l_1 + \Delta l_2$ is considered in order to account for the radiation at the discontinuity between the neck and the cavity, Δl_1 [42], and the radiation between the neck and the waveguide, Δl_2 [43].

$$\Delta l = 0.41 \left[1 - 1.35 \frac{w_n}{w_c} + 0.31 \left(\frac{w_n}{w_c} \right)^3 \right] w_n + 0.41 \left[1 - 0.235 \frac{w_n}{h} - 1.321 \left(\frac{w_n}{h} \right)^2 + 1.54 \left(\frac{w_n}{h} \right)^3 - 0.86 \left(\frac{w_n}{h} \right)^4 \right] w_n. \tag{A6}$$

Another correction length to consider is the radiation from the slit to the external waveguide

$$\Delta l_{\text{slit}} = \frac{h^2}{w_{\text{ex}}} \sum_{n=1}^{\infty} \frac{\sin^2(n\pi h/w_{\text{ex}})}{(n\pi h/w_{\text{ex}})^3}, \tag{A7}$$

which allows to define the length correction matrix

$$\mathbf{T}_{\Delta l_{\text{slit}}} = \begin{bmatrix} 1 & -i\omega \Delta l_{\text{slit}} \rho_{\text{ex}} w_{\text{ex}}/h S_{\text{ex}} \\ 0 & 1 \end{bmatrix}. \tag{A8}$$

If a Neuman condition (rigid backing) is applied on the opposite side of the input, the total reflection coefficient of the rigidly backed metasurface can be calculated from the transfer matrix elements as

$$R_{\text{TMM}} = \frac{\mathbf{t}_{11} - Z_{\text{ex}} \mathbf{t}_{21}}{\mathbf{t}_{11} + Z_{\text{ex}} \mathbf{t}_{21}}. \tag{A9}$$

In the case of a transmission configuration, the transfer matrix is simply multiplied by its symmetric, and the reflection $|R|$ and transmission $|T|$ coefficients read as follows:

$$T = \frac{2}{t_{11} + (t_{12}/Z_{ex}) + Z_{ex}t_{21} + t_{22}}, \tag{A10}$$

and

$$R = \frac{t_{11} + (t_{12}/Z_{ex}) - Z_{ex}t_{21} - t_{22}}{(t_{12}/Z_{ex}) + Z_{ex}t_{21} + t_{22}}, \tag{A11}$$

for a symmetric $T_{11} = T_{22}$ and reciprocal $T_{11}T_{22} - T_{12}T_{21} = 1$ system.

APPENDIX B: VISCOTHERMAL LOSSES MODELING

The viscothermal losses are accounted for in each part of the system, i.e., in the cavity and the neck of the resonators, in the slit above, and in the external waveguide. The viscothermal losses are modeled using the complex and frequency-dependent impedance $Z(\omega) = \kappa(\omega)\rho(\omega)/S$ and wave number $k(\omega)$ [44].

The cavities and the necks are considered as slits since their width is greater than their other dimensions. Their complex density $\rho(\omega)$ and bulk modulus $\kappa(\omega)$ are therefore as follows:

$$\rho(\omega) = \rho_0 \left[1 - \frac{\tanh(G_\rho w/2)}{G_\rho w/2}\right]^{-1}, \tag{B1}$$

$$\kappa(\omega) = \kappa_0 \left[1 + (\gamma - 1)\frac{\tanh(G_\kappa w/2)}{G_\kappa w/2}\right]^{-1}; \tag{B2}$$

with $G_\rho = \sqrt{i\omega\rho_0/\mu_0}$ and $G_\kappa = \sqrt{i\omega Pr\rho_0/\mu_0}$, where Pr is the Prandtl number, μ the dynamic viscosity, ρ_0 the air density, $\kappa_0 = \gamma P_0$ the air bulk modulus, γ the specific heat ratio, and P_0 the atmospheric pressure.

The complex density and bulk modulus of the outer waveguide are modeled as those of a rectangular waveguide of widths $q_1 = q_2 = w_{ex}/2$

$$\rho(\omega) = -\frac{\rho_0 q_1^2 q_2^2}{4G_\rho^2 \sum_{n\in\mathbb{N}} \sum_{m\in\mathbb{N}} \left[\alpha_n^2\beta_m^2\left(\alpha_n^2 + \beta_m^2 - G_\rho^2\right)\right]^{-1}}, \tag{B3}$$

$$\kappa(\omega) = \frac{\kappa_0}{\gamma + \frac{4(\gamma-1)G_\kappa^2}{q_1^2 q_2^2} \sum_{n\in\mathbb{N}} \sum_{m\in\mathbb{N}} \left[\alpha_n^2\beta_m^2\left(\alpha_n^2 + \beta_m^2 - G_\kappa^2\right)\right]^{-1}}, \tag{B4}$$

where $\alpha_n = 2(n + 1/2)\pi/q_1$ and $\beta_m = 2(m + 1/2)\pi/q_2$.

APPENDIX C: DISPERSION RELATION

1. Dispersion relation: one single unit cell

The dispersion relation of an infinite periodic system can be calculated directly from the transfer matrix of a single unit cell

$$k(\omega)a = \cos^{-1}\left[\frac{t_{11} + t_{12}}{2}\right]. \tag{C1}$$

2. Effective properties of a finite size material

The dispersion relation does not include the effect of the finite number of unit cells. Another option is to determine the effective properties using the transmission and reflection coefficients of the finite system [45].

The derivation of the effective impedance is fairly straightforward

$$Z(\omega) = \pm Z_0 \sqrt{\frac{(1+R)^2 - T^2}{(1-R)^2 - T^2}}, \tag{C2}$$

while the effective wave number

$$k(\omega) = -\frac{\ln(|e^{ik(\omega)L}|) + i\arg(e^{ik(\omega)L})}{iL} + \frac{2\pi m}{L}, \tag{C3}$$

results from the inversion of

$$e^{ik(\omega)L} = \frac{T[1 - Z(\omega)/Z_{ex}]}{R[1 + Z(\omega)/Z_{ex}] - Z(\omega)/Z_{ex} + 1}, \tag{C4}$$

with m a natural integer to correct the phase after inversion, the exponential being 2π periodic.

[1] M. R. Schroeder, Diffuse sound reflection by maximum length sequences, J. Acoust. Soc. Am. 57, 149 (1975).

[2] J. Jagla, P. Chervin, and J. Martin, Carmen and Carmencita electroacoustic systems (2017) p. 3852.

[3] X. Guo, H. Lissek, and R. Fleury, Improving Sound Absorption Through Nonlinear Active Electroacoustic Resonators, Phys. Rev. Appl. **13**, 014018 (2020).

[4] C. Cho, X. Wen, N. Park, and J. Li, Digitally virtualized atoms for acoustic metamaterials, Nat. Commun. **11**, 251 (2020).

[5] T. S. Becker, D.-J. Van Manen, C. M. Donahue, C. Barlocher, N. Borsing, F. Broggini, T. Haag, J. O. Robertsson, D. R. Schmidt, S. A. Greenhalgh, and T. E. Blum, Immersive Wave Propagation Experimentation: Physical Implementation and One-Dimensional Acoustic Results, Phys. Rev. X **8**, 031011 (2018).

[6] X. Li, J. Robertsson, A. Curtis, and D.-J. van Manen, Compensating for source directivity in immersive wave experimentation, J. Acoust. Soc. Am. **146**, 3141 (2019).

[7] T. S. Becker, N. Borsing, T. Haag, C. Barlocher, C. M. Donahue, A. Curtis, J. O. A. Robertsson, and D.-J. van Manen, Real-Time Immersion of Physical Experiments in Virtual Wave-Physics Domains, Phys. Rev. Appl. **13**, 064061 (2020).

[8] T. Cavalieri, J. Boulvert, G. Gabard, V. Romero-García, M. Escouflaire, J. Regnard, and J.-P. Groby, Graded and anisotropic porous materials for broadband and angular maximal acoustic absorption, Materials **13**, 4605 (2020).

[9] B. Assouar, B. Liang, Y. Wu, Y. Li, J.-C. Cheng, and Y. Jing, Acoustic metasurfaces, Nat. Rev. Mater. **3**, 460 (2018).

[10] M. Yang and P. Sheng, Sound absorption structures: From porous media to acoustic metamaterials, Annu. Rev. Mater. Res. **47**, 83 (2017).

[11] N. Jimenez, V. Romero-García, V. Pagneux, and J.-P. Groby, Rainbow-trapping absorbers: Broadband, perfect and asymmetric sound absorption by subwavelength panels for transmission problems, Sci. Rep. **7**, 13595 (2017).

[12] E. Ballestero, N. Jimenez, J.-P. Groby, S. Dance, H. Aygun, and V. Romero-García, Experimental validation of deep-subwavelength diffusion by acoustic metadiffusers, Appl. Phys. Lett. **115**, 081901 (2019).

[13] S. Qu and P. Sheng, Minimizing Indoor Sound Energy with Tunable Metamaterial Surfaces, Phys. Rev. Appl. **14**, 034060 (2020).

[14] Y. Zhu, A. Merkel, K. Donda, S. Fan, L. Cao, and B. Assouar, Nonlocal acoustic metasurface for ultrabroadband sound absorption, Phys. Rev. B **103**, 064102 (2021).

[15] M. Yang, S. Chen, C. Fu, and P. Sheng, Optimal sound-absorbing structures, Mater. Horiz. **4**, 673 (2017).

[16] H. Y. Mak, X. Zhang, Z. Dong, S. Miura, T. Iwata, and P. Sheng, Going beyond the Causal Limit in Acoustic Absorption, Phys. Rev. Appl. **16**, 044062 (2021).

[17] X. Cai, Q. Guo, G. Hu, and J. Yang, Ultrathin low-frequency sound absorbing panels based on coplanar spiral tubes or coplanar Helmholtz resonators, Appl. Phys. Lett. **105**, 121901 (2014).

[18] M. Yang, C. Meng, C. Fu, Y. Li, Z. Yang, and P. Sheng, Subwavelength total acoustic absorption with degenerate resonators, Appl. Phys. Lett. **107**, 104104 (2015).

[19] N. Jimenez, V. Romero-García, V. Pagneux, and J.-P. Groby, Quasiperfect absorption by subwavelength acoustic panels in transmission using accumulation of resonances due to slow sound, Phys. Rev. B **95**, 014205 (2017).

[20] T. Lee, T. Nomura, E. M. Dede, and H. Iizuka, Ultrasparse Acoustic Absorbers Enabling Fluid Flow and Visible-Light Controls, Phys. Rev. Appl. **11**, 024022 (2019).

[21] V. Romero-García, N. Jimenez, J.-P. Groby, A. Merkel, V. Tournat, G. Theocharis, O. Richoux, and V. Pagneux, Perfect Absorption in Mirror-Symmetric Acoustic Metascreens, Phys. Rev. Appl. **14**, 054055 (2020).

[22] V. Romero-García, G. Theocharis, O. Richoux, A. Merkel, V. Tournat, and V. Pagneux, Perfect and broadband acoustic absorption by critically coupled sub-wavelength resonators, Sci. Rep. **6**, 19519 (2016).

[23] N. Jimenez, W. Huang, V. Romero-García, V. Pagneux, and J.-P. Groby, Ultra-thin metamaterial for perfect and quasi-omnidirectional sound absorption, Appl. Phys. Lett. **109**, 121902 (2016).

[24] Y. Auregan, Ultra-thin low frequency perfect sound absorber with high ratio of active area, Appl. Phys. Lett. **113**, 201904 (2018).

[25] J. Mei, G. Ma, M. Yang, Z. Yang, W. Wen, and P. Sheng, Dark acoustic metamaterials as super absorbers for low-frequency sound, Nat. Commun. **3**, 756 (2012).

[26] P. Wei, C. Croënne, S. Tak Chu, and J. Li, Symmetrical and anti-symmetrical coherent perfect absorption for acoustic waves, Appl. Phys. Lett. **104**, 121902 (2014).

[27] M. Yang, Y. Li, C. Meng, C. Fu, J. Mei, Z. Yang, and P. Sheng, Sound absorption by subwavelength membrane structures: A geometric perspective, C. R. Mecanique **343**, 635 (2015).

[28] V. Leroy, A. Strybulevych, M. Lanoy, F. Lemoult, A. Tourin, and J. H. Page, Superabsorption of acoustic waves with bubble metascreens, Phys. Rev. B **91**, 020301 (2015).

[29] M. Lanoy, R.-M. Guillermic, A. Strybulevych, and J. H. Page, Broadband coherent perfect absorption of acoustic waves with bubble metascreens, Appl. Phys. Lett. **113**, 171907 (2018).

[30] V. Romero-García, G. Theocharis, O. Richoux, and V. Pagneux, Use of complex frequency plane to design broadband and sub-wavelength absorbers, J. Acoust. Soc. Am. **139**, 3395 (2016).

[31] V. Romero-García, N. Jimenez, G. Theocharis, V. Achilleos, A. Merkel, O. Richoux, V. Tournat, J.-P. Groby, and V. Pagneux, Design of acoustic metamaterials made of Helmholtz resonators for perfect absorption by using the complex frequency plane, C. R. Phys. **21**, 713 (2021).

[32] Y. Li and B. M. Assouar, Acoustic metasurface-based perfect absorber with deep subwavelength thickness, Appl. Phys. Lett. **108**, 063502 (2016).

[33] C. Zhang and X. Hu, Three-Dimensional Single-Port Labyrinthine Acoustic Metamaterial: Perfect Absorption with Large Bandwidth and Tunability, Phys. Rev. Appl. **6**, 064025 (2016).

[34] K. Donda, Y. Zhu, S.-W. Fan, L. Cao, Y. Li, and B. Assouar, Extreme low-frequency ultrathin acoustic absorbing metasurface, Appl. Phys. Lett. **115**, 173506 (2019).

[35] J.-P. Groby, R. Pommier, and Y. Auregan, Use of slow sound to design perfect and broadband passive sound absorbing materials, J. Acoust. Soc. Am. **139**, 1660 (2016).

[36] J.-P. Groby, W. Huang, A. Lardeau, and Y. Auregan, The use of slow waves to design simple sound absorbing materials, J. Appl. Phys. **117**, 124903 (2015).
[37] Y. Zhu, X. Fan, B. Liang, J. Cheng, and Y. Jing, Ultrathin Acoustic Metasurface-Based Schroeder Diffuser, Phys. Rev. X **7**, 021034 (2017).
[38] N. Jimenez, T. J. Cox, V. Romero-García, and J.-P. Groby, Metadiffusers: Deep-subwavelength sound diffusers, Sci. Rep. **7**, 5389 (2017).
[39] E. Ballestero, N. Jimenez, J.-P. Groby, H. Aygun, S. Dance, and V. Romero-García, Metadiffusers for quasi-perfect and broadband sound diffusion, Appl. Phys. Lett. **119**, 044101 (2021).
[40] A. N. Norris, Acoustic metafluids, J. Acoust. Soc. Am. **125**, 839 (2009).
[41] G. Theocharis, O. Richoux, V. R. García, A. Merkel, and V. Tournat, Limits of slow sound propagation and transparency in lossy, locally resonant periodic structures, New J. Phys. **16**, 093017 (2014).
[42] J. Kergomard and A. Garcia, Simple discontinuities in acoustic waveguides at low frequencies: Critical analysis and formulae, J. Sound. Vib. **114**, 465 (1987).
[43] V. Dubos, J. Kergomard, A. Khettabi, J.-P. Dalmont, D. H. Keefe, and C. J. Nederveen, Theory of sound propagation in a duct with a branched tube using modal decomposition, Acta Acust. United Acust. **85**, 153 (1999).
[44] M. R. Stinson, The propagation of plane sound waves in narrow and wide circular tubes, and generalization to uniform tubes of arbitrary cross-sectional shape, J. Acoust. Soc. Am **89**, 550 (1991).
[45] D. R. Smith, S. Schultz, P. Markos, and C. M. Soukoulis, Determination of effective permittivity and permeability of metamaterials from reflection and transmission coefficients, Phys. Rev. B **65**, 195104 (2002).